ROM SAF Report 26
Ref: SAF/ROM/METO/REP/RSR/026
Web: www.romsaf.org
Date: 23 August 2016

The EUMETSAT Network of Satellite Application Facilities

ROM SAF
Radio Occultation Meteorology

ROM SAF Report 26

Estimates of GNSS radio occultation bending angle and refractivity error statistics

Sean Healy

ECMWF

Document Author Table

	Name	Function	Date	Comments
Prepared by:	S. Healy	ROM SAF Project Team	23 August 2016	
Reviewed by:	C. Burrows	ROM SAF Project Team	22 July 2016	
Reviewed by:	-	-	-	
Approved by:	K. B. Lauritsen	ROM SAF Project Manager	29 July 2016	

Document Change Record

Issue/Revision	Date	By	Description
-	-	-	

ROM SAF

The Radio Occultation Meteorology Satellite Application Facility (ROM SAF) is a decentralised processing centre under EUMETSAT which is responsible for operational processing of GRAS radio occultation data from the Metop satellites and RO data from other missions. The ROM SAF delivers bending angle, refractivity, temperature, pressure, and humidity profiles in near-real time and offline for NWP and climate users. The offline profiles are further processed into climate products consisting of gridded monthly zonal means of bending angle, refractivity, temperature, humidity, and geopotential heights together with error descriptions.

The ROM SAF also maintains the Radio Occultation Processing Package (ROPP) which contains software modules that will aid users wishing to process, quality-control and assimilate radio occultation data from any radio occultation mission into NWP and other models.

The ROM SAF Leading Entity is the Danish Meteorological Institute (DMI), with Cooperating Entities: i) European Centre for Medium-Range Weather Forecasts (ECMWF) in Reading, United Kingdom, ii) Institut D'Estudis Espacials de Catalunya (IEEC) in Barcelona, Spain, and iii) Met Office in Exeter, United Kingdom. To get access to our products or to read more about the project please go to: http://www.romsaf.org

Intellectual Property Rights

Abstract

The ECMWF numerical weather prediction (NWP) system has been used to estimate the GNSS radio occultation bending angle error statistics from Metop GRAS and COSMIC measurements. These statistics have been mapped to refractivity space using a linear Abel transform. We have found that the broader vertical bending angle error correlations for rising GRAS measurements account for most of the difference between the rising and setting refractivity profile statistics. The senstivity of the refractivity results to bending angle error correlations is demonstrated and discussed. The importance of modelling the refractivity error correlations correctly is emphasised. The results also suggest that the refractivity error model used in the ROM SAF 1D-Var should be revisited.

Contents

1 Background and Main Results

1.1 Introduction

Assimilating observations into numerical weather prediction (NWP) systems can provide useful information about the characteristics of the observed data. The assimilated observations have passed strict quality control criteria, and in the forward modelling to observation space, the NWP model integration to the time and location of the observation minimizes collocation errors. The NWP system subsequently produces useful diagnostics based on the analysis. For example, in addition to computing the standard observation minus background (o-b) statistics, we can estimate observation error statistics (Desrozier *et al.*, 2005). This information can potentially be used to improve ROM SAF products, which are dependent on a good understanding of the information content and error characteristics of the measurements.

In this work, we have used the ECMWF NWP system to provide estimates of the GNSS radio occultation (GNSS-RO) bending angle error covariance matrices for both GRAS and COSMIC measurements. We have found that the bending angle variability is close to the assumed errors near 50 km, indicating that the GNSS-RO measurements are unlikely to have any significant impact on random forecast errors at this height, unless there is a large reduction in observation errors in future missions. The general shape of the GRAS vertical error correlations presented in this work is well known. However, there are clear differences between the rising and setting GRAS bending angle error correlations below 20 km. Although the GRAS error correlations are not large, it is shown that they have a significant impact when the bending angle error statistics are mapped to refractivity space. The rising/setting correlation differences account for most of the difference in GRAS rising/setting refractivity statistics in the 10-20 km vertical interval. The present results also suggest that the error model used in the ROM SAF 1D-Var calculations should be revised, with a potentially different matrix used for rising and setting observations.

1.2 Estimation of observation error statistics

Desrozier *et al.* (2005) have shown that departure statistics from assimilation experiments provide an *estimate* of the observation error covariance matrix, $\mathbf{R_D}$. More specifically, we can compute

$$\mathbf{R_D} = \overline{(\mathbf{y_m} - \mathbf{H}(\mathbf{x_b}))(\mathbf{y_m} - \mathbf{H}(\mathbf{x_a}))^{\mathbf{T}}} \tag{1.1}$$

where $\mathbf{x_b}$ and $\mathbf{x_a}$ are the forecast and analysis, respectively, $\mathbf{H}$ is the bending angle forward model and $\mathbf{y_m}$ is the observation vector. This can be written in an alternative form, in terms of the assumed and true error covariance matrices, which illustrates the nature of the solution. Let $\mathbf{B_t}$ and $\mathbf{R_t}$ be the unknown, "true" background and observation error covariance matrices, respectively, and let the assumed covariance matrices – used in the assimilation of the

GNSS-RO data – be defined here as $\mathbf{B_a} = \mathbf{B_t} - \delta\mathbf{B}$ and $\mathbf{R_a} = \mathbf{R_t} - \delta\mathbf{R}$. Eq. 1.1 can then be written as,

$$\mathbf{R_D} = \mathbf{R_a}(\mathbf{H}\mathbf{B_a}\mathbf{H^T} + \mathbf{R_a})^{-1}(\mathbf{R_t} + \mathbf{H}(\delta\mathbf{B})\mathbf{H^T}) + \mathbf{H}\mathbf{B_a}\mathbf{H^T}(\mathbf{H}\mathbf{B_a}\mathbf{H^T} + \mathbf{R_a})^{-1}\mathbf{R_a} \quad (1.2)$$

Two limiting cases are apparent. Firstly, if the assumed observation error covariance matrix is much "larger" [1] than the assumed background errors mapped to bending angle space, then $\mathbf{R_D}$ will tend to $\mathbf{R_D} \simeq \mathbf{R_t} + \mathbf{H}(\mathbf{B_a} + \delta\mathbf{B_a})\mathbf{H^T} = \mathbf{R_t} + \mathbf{H}\mathbf{B_t}\mathbf{H^T}$. Conversely, if the assumed bending angle errors are much smaller than the assumed background errors mapped to bending angle space, then $\mathbf{R_D}$ will tend to the assumed matrix, $\mathbf{R_D} \simeq \mathbf{R_a}$. In addition, the computed $\mathbf{R_D}$ is not generally symmetric. Nevertheless, the approach is useful for updating and improving the assumed observation error covariance matrix, $\mathbf{R_a}$, used to assimilate the data. It provides an alternative method for estimating error covariance matrices, which complements the error propagation studies (e.g., see Kursinski *et al.* 1997; Syndergaard 1999; Steiner and Kirchengast 1999; Steiner and Kirchengast, 2005), and it has been used previously for GNSS-RO applications by Poli *et al.* (2009).

1.3 Bending angle error statistics

The assumed error covariance matrix, $\mathbf{R_a}$, used to assimilate the GNSS-RO data is a global model, and vertical correlations are not included. The percentage bending angle errors are given as a function of impact height, h, which is defined as impact parameter minus radius of curvature $(a - r_c)$. They fall linearly from 20 $\%$ at h=0 to 1% at h=10 km. The errors above 10 km are then 1% until this reaches a lower absolute limit of 3 microradians.

Figure 1.1 shows the vertical profile of the standard deviation of the estimated bending angle errors for Metop-A GRAS setting occultations, in the northern hemisphere, tropics and southern hemisphere computed with Eq.1.1. The vertical interval is between impact heights of 10 km and 35 km. The statistics are derived for the period January 1–31, 2015, and they are computed on the standard Metop GRAS levels found in the operational BUFR files. Given the use of $\mathbf{H}(\mathbf{x_a})$ in Eq.1.1, by definition the statistics are computed from bending angles that have passed the NWP quality control, and are actively assimilated. The uncertainty estimates are larger than the values provided by Steiner and Kirchengast (2005), who found $\sim 0.5\%$ in this interval. Figure 1.1 also illustrates a latitudinal dependence in the estimated error statistics, which is not currently accounted for in the operational assimilation of this data at ECMWF. The larger errors estimates in the tropics between 15 - 20 km are related to the variability around the tropical tropopause and gravity waves. For comparison, Figure 1.2 shows the variability of the observed (solid) and forward modeled (dotted) bending angles about their respective mean profiles up to 50 km. The larger variability in the northern hemisphere than in the southern hemisphere above $\sim$ 22 km is related to vertically propagating planetary waves in the winter hemisphere. The overall consistency between the observed and forward modeled bending angle variability below 30 km is encouraging, but it is by construction to some extent, since the observed minus modeled bending angle differences must pass the NWP quality control measures for active assimilation. The divergence between the model and observed variability above $\sim$ 35 km can be attributed to the observation errors, which begin to contribute a significant fraction of the observed bending angle variability. The

[1] Assume a symmetric matrix **A** is "larger" than the symmetric matrix **B** if $\mathbf{A} - \mathbf{B}$ is positive definite.

Table 1.1: The estimated standard deviation of the bending angle errors, and the observed and forward modeled bending angle variability. The vertical level is near 50 km and the units are microradians. ECMWF assumes the standard deviation of the bending angle errors is 3 microradians near 50 km.

Area	Mean observed value	Error estimate	Observed Variability	Modeled variability
NH	15.7	2.0	2.6	1.7
TR	17.3	2.0	2.0	0.6
SH	19.4	2.3	2.5	0.9

standard deviations of the estimated Metop-A GRAS bending angle errors near 50 km, and the observed and forward modeled variability estimates are given in Table 1.1. Clearly, the uncertainty estimates are close to the observed bending angle variability values, and larger than the variability of the forward modeled bending angles. The NWP model state near 50 km will be primarily constrained by AMSU-A channel 14 radiances.

Assuming that NWP short-range forecast errors are significantly smaller than the natural variability, and that the computed observation uncertainty is a reasonable estimate of the actual value, Table 1.1 clearly illustrates the limited information content of GNSS-RO measurements at these heights. In fact, the GNSS-RO measurements are unlikely to have any significant NWP impact on random errors in the upper-stratosphere and mesosphere, unless random measurement errors can be reduced to below the ~ 0.1 microradian level. The GNSS-RO measurements may still have a role constraining biases at these levels. These results also have some possible implications for the use of climatological mean profiles in the statistical optimization, since the spatial variation in the bending angle variability should be accounted for in the statistical optimization process, when computing the linear combination of the observed and climatological bending angles.

We can compare both the Metop and COSMIC error estimates, and the statistical differences associated with rising and setting measurements (Figure 1.3). These results are for the northern hemisphere, but the results in the tropics and southern hemisphere are qualitatively similar. It is clear that COSMIC measurements have considerably smaller uncertainty estimates, and that the Metop-A and Metop-B results are consistent with each other. The rising occultations tend to have larger errors in the 10-20 km interval for Metop-A and Metop-B, but the rising/setting differences are smaller for COSMIC data. A contributing factor to the better COSMIC error estimates is an additional smoothing step applied to the bending angles available in the BUFR files. UCAR apply a Gaussian smoother, with a full width at half maximum (FWHM) of ~ 200 m, to the corrected bending angles before the data is thinned for inclusion in the BUFR files (Sokolovskiy, Pers. Comm). In contrast, EUMETSAT linearly interpolate the high-resolution data to the 247 BUFR levels, although this will change as a result of processing updates in July, 2016. UCAR also employ a stricter quality control procedure, and this may also have some affect on the differences.

It is useful to write a covariance matrix as the product of a symmetric correlation matrix, $\mathbf{C}$, and a diagonal matrix, $\mathbf{D}$, which contains the standard deviation estimates ($\mathbf{R} = \mathbf{DCD}$). Vertical correlations in the bending angle errors are not currently included when assimilating the data at ECMWF, so it assumed $\mathbf{C} = \mathbf{I}$. Including vertical error correlations has been tested previously (Healy, 2008). However, they are more difficult to introduce now because tangent

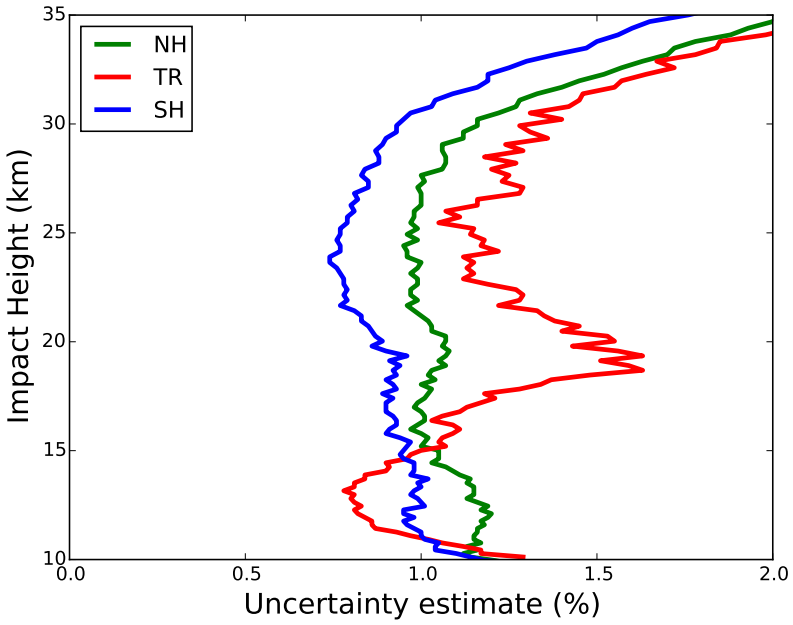

Figure 1.1: The standard deviation of the observation errors (uncertainty) in the NH, TR and SH for setting Metop-A GRAS measurements. The period is January 1-31, 2015, and the results are shown as a percentage of the mean bending angle profiles for each area.

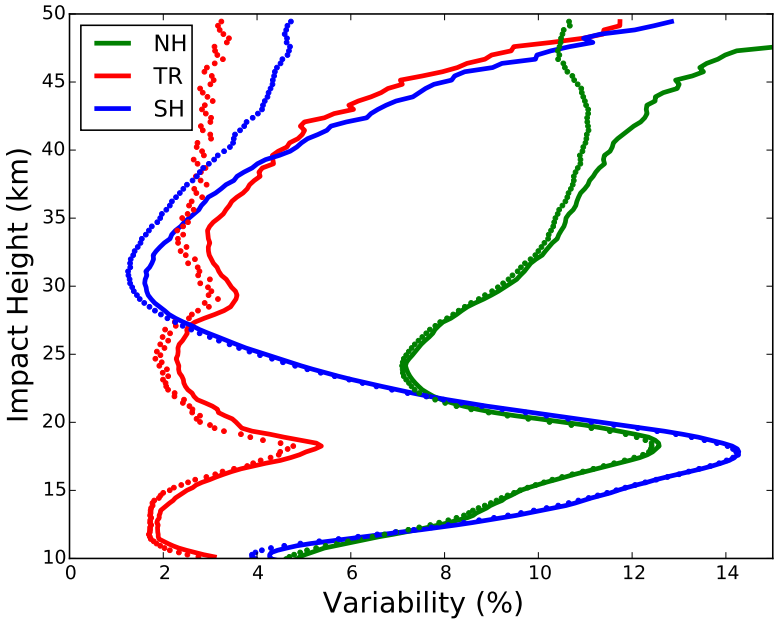

Figure 1.2: The observed and forward modeled bending angle variability values for the Metop-A setting measurements. The results for the observed (solid) and forward modeled (dotted) values are plotted as a percentage of the respective observed and modeled mean profiles.

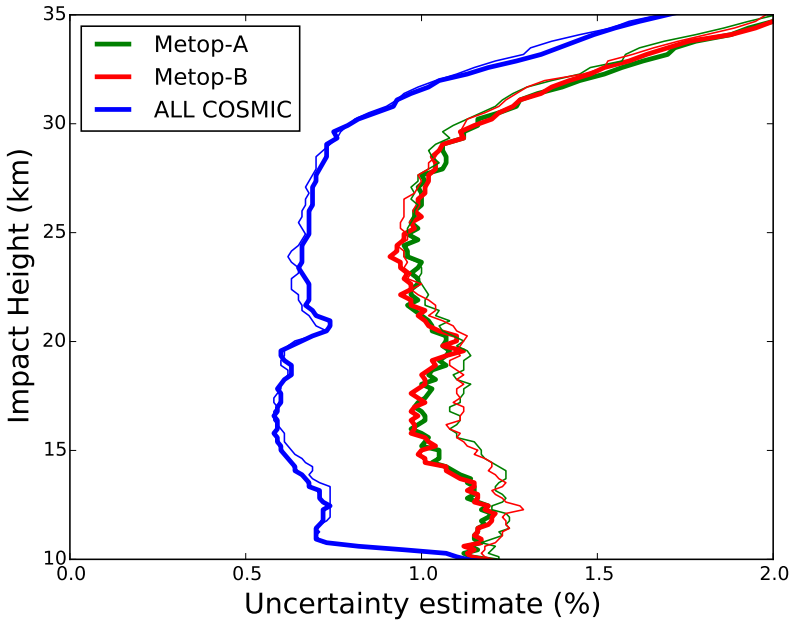

Figure 1.3: The estimated standard deviation of the bending angle errors for the Metop-A, Metop-B and the COSMIC radio occultation measurements in the northern hemisphere. The thick lines are for setting occultations and the thin lines are for rising occultations.

point drift is modeled, and this would require both horizontal and vertical observation error correlations to be condidered.

Estimates of the vertical error correlations for bending angles near 13 km in the northern hemisphere for setting and rising occultations are shown in Figure 1.4 and Figure 1.5, respectively. The Metop correlations shown in Figure 1.4 are physically plausible, and have a familiar pattern/structure which has been noted previously (e.g., see Syndergaard, 1999; Steiner and Kirchengast, 2005; Poli *et al.*, 2007). The correlation structure arises from the combination of the differentiation of the excess phase delays, which produces negative lobes in the correlation function, and a smoothing step. EUMETSAT currently smooth 75 excess delay values sampled at 50 Hz, resulting in a smoothing time interval of 1.5 s. In contrast, the COSMIC correlations for setting measurements are broader and generally positive. This may be partly a result of the additional smoothing of COSMIC bending angles noted above, and perhaps the result of error propagation through the Full Spectrum Inversion (FSI) (Jensen *et al.* 2003). However, more work is required to clarify this issue. The correlations for rising measurements (Figure 1.5) are generally positive and broader in this vertical interval. In particular, the correlations of the Metop measurements do not fall to zero, instead falling to $\sim$ 0.2 at 20 km. This is related to the fact that for rising occulations the L2 measurements start at only 20 km, and the corrected bending angles below 20 km are based on extrapolated L1-L2 model, based on fitting the measurements above 20 km. This has been confirmed by comparing the Metop-A and Metop-B correlations in May 2013, before this approach was implemented in the Metop-A processing.

The error correlation estimates for bending angles from setting occultations at 23 km and

34 km are shown in Figure 1.6 and Figure 1.7, respectively. The consistency between error correlations for rising and setting occultations is much better at these heights, and so the rising measurements are not shown here. It is notable that the GRAS correlations appear to narrow significantly as the measurements get lower in the atmosphere. This was discussed by Syndergaard (1999), and it is related to the fact that excess phase delay smoothing is over a fixed time interval which, as noted above, is 1.5 s for GRAS processing. The change in impact parameter over a fixed time interval reduces as the measurement penetrates deeper into the atmosphere, and this produces the apparent narrowing of the vertical correlations when plotted as a function of impact height. The variation of the COSMIC correlations with height is less pronounced.

It is important to note that the general bending angle correlation structure – a sharp peak and negative lobes – is well known, and is generally accepted. However, this correlation structure is not fundamental to the processing, and perhaps it need not impact the thinned data available for NWP assimilation. In the geometrical optics processing, the time derivative of the excess phase delays is a necessary step, but the differentiation of 50 Hz data alone would only result in vertical correlations of a few 10's of metres. For example, consider the case where the excess phase delay errors are uncorrelated, and characterized by the uncertainty estimate, σ_ϕ. The derivative matrix, $\mathbf{G}$, based on the forward finite difference approximation, can be written as,

$$\mathbf{G} = \frac{1}{\Delta t} \begin{pmatrix} -1 & 1 & 0 & 0 & 0 & & & & & \\ 0 & -1 & 1 & 0 & 0 & & & & & \\ 0 & 0 & -1 & 1 & 0 & & & & & \\ & & & & \cdots & & & & & \\ & & & & & 0 & -1 & 1 & 0 & 0 \\ & & & & & 0 & 0 & -1 & 1 & 0 \\ & & & & & 0 & 0 & 0 & -1 & 1 \end{pmatrix} \tag{1.3}$$

where $\Delta t = 1/50$ s. The covariance matrix of the Doppler shifts is then proportional to $\mathbf{G}\mathbf{G}^{\mathbf{T}}$ (See also, Syndergaard (1999) for corresponding matrices but assuming the centred finite difference derivative),

$$\mathbf{R}_{\mathbf{Dopp}} \propto \frac{\sigma_\phi^2}{\Delta t^2} \begin{pmatrix} 2 & -1 & 0 & 0 & 0 & & & & & \\ -1 & 2 & -1 & 0 & 0 & & & & & \\ 0 & -1 & 2 & -1 & 0 & & & & & \\ & & & & \cdots & & & & & \\ & & & & & 0 & -1 & 2 & -1 & 0 \\ & & & & & 0 & 0 & -1 & 2 & -1 \\ & & & & & 0 & 0 & 0 & -1 & 2 \\ . & & & & & & & & & \end{pmatrix} \tag{1.4}$$

Hence, the broadening of the Doppler and bending angle correlations of the order a few kilometres must be primarily determined by the width of smoothing interval. If this interval was reduced to $\sim$ 100 m, the negative correlations of the thinned data available for NWP

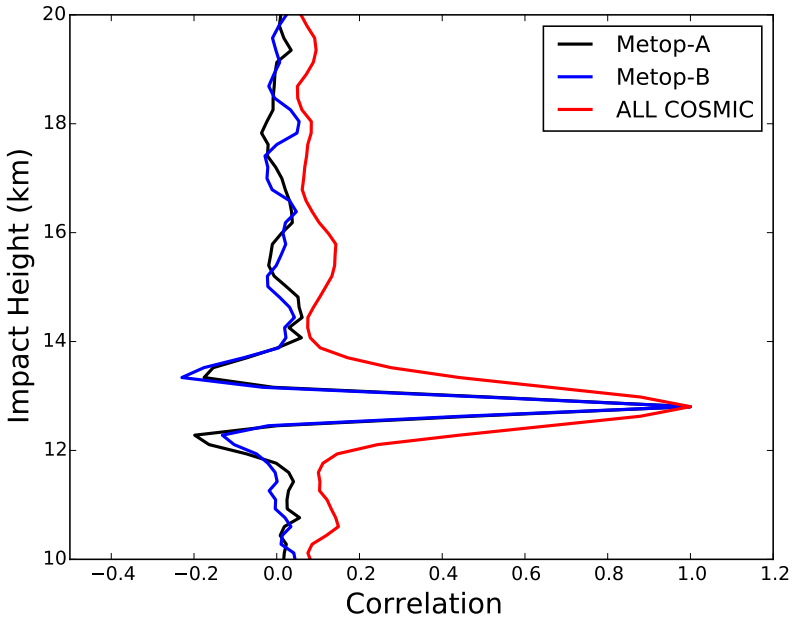

Figure 1.4: . The bending angle error correlation estimates for setting observations near 13 km in the northern hemisphere.

could be removed. However, it would be at the expense of higher random noise, and so the trade-off should be investigated.

We can also use this technique to estimate the bending angle observation error statistics in the lower troposphere using the COSMIC measurements. Figure 1.8 shows the error estimates computed with both a two dimensional (2D) observation operator (thick lines) and a one dimensional (1D) observation operator (thin lines). Noting that Eq.1.1 produces an estimate of the combined forward model and observation error covariance matrix, $\mathbf{R}$, the difference between the 1D and 2D results can be interpreted as a reduction in forward model error. The forward model error reduction is reasonably clear in the both northern and – to a greater extent – southern hemisphere region, but less so in the tropics. This requires further investigation, but it should be noted that the 2D operator reduces (o-b) bending angle departure statistics globally. There is a clear seasonal signal in the error statistics for both the 1D and 2D operators, with larger errors in the southern hemisphere, which is warmer and moister. This suggests a tropospheric observation error model related to the total column water at the observation location is worth considering.

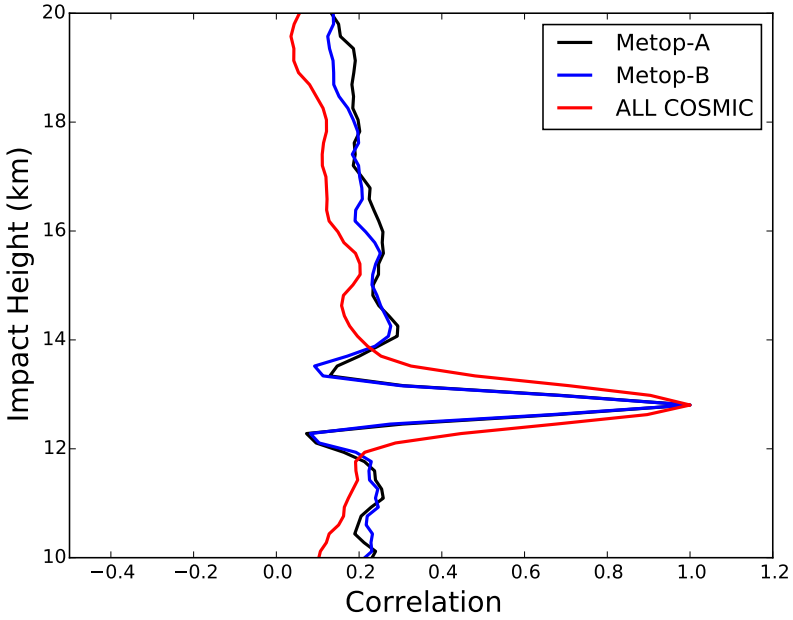

Figure 1.5: . The bending angle error correlation estimates for rising observations near 13 km in the northern hemisphere.

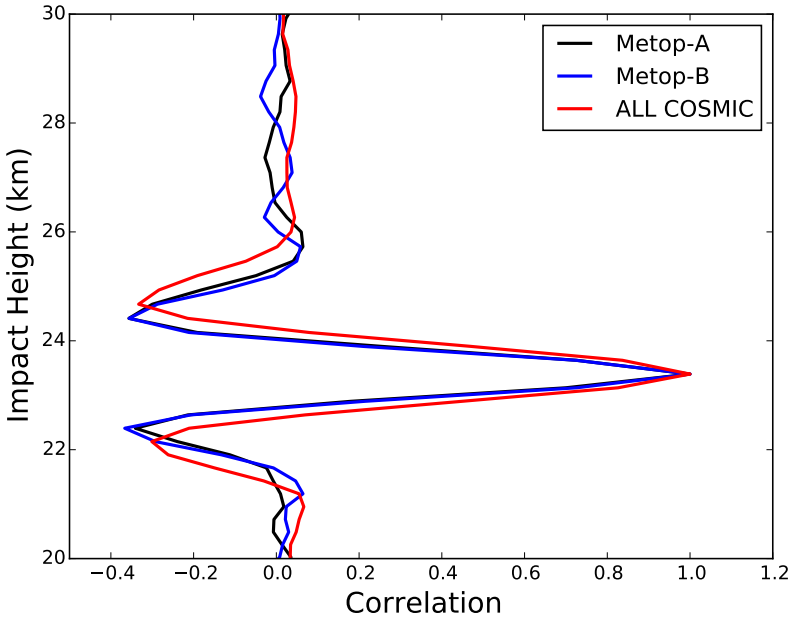

Figure 1.6: . The bending angle error correlation estimates for setting observations near 23 km in the northern hemisphere.

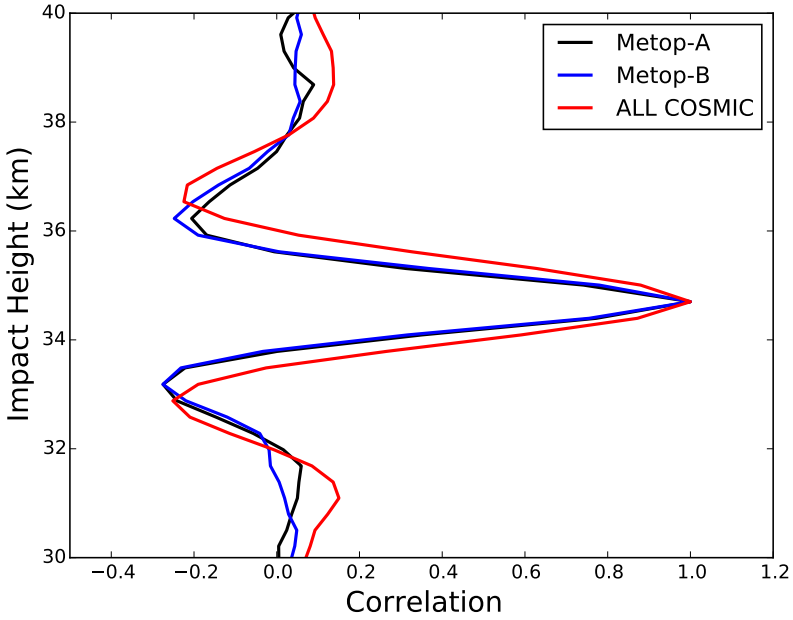

Figure 1.7: The bending angle error correlation estimates for setting observations near 34 km in the northern hemisphere.

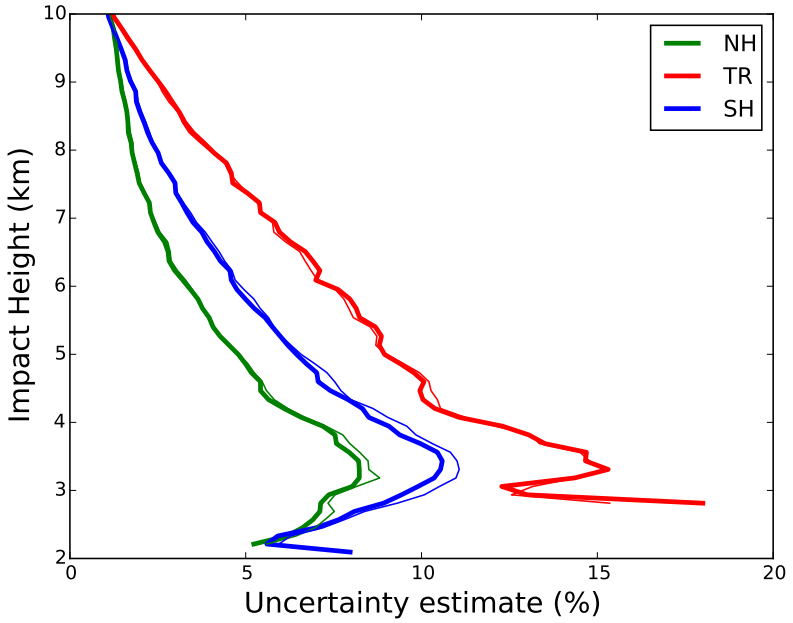

Figure 1.8: The bending angle error estimates in the troposphere for the COSMIC measurements. The thick lines are using a 2D observation operator and the thin lines are using a 1D observation operator.

1.4 Implied refractivity error statistics

The main motivation for assimilating bending angles rather than refractivity is that the error characteristics should be simpler. ECMWF does not assimilate refractivity, or routinely compute refractivity departure statistics. However, the "implied" refractivity error covariance matrix, $\mathbf{R_N}$, can be estimated by propagating the bending angle error covariance matrix, $\mathbf{R_D}$, through a linearized Abel transform matrix, $\mathbf{A}$, (See Eq. 3.33, Syndergaard, 1999) giving,

$$\mathbf{R_N} \simeq \mathbf{A}\mathbf{R_D}\mathbf{A^T}. \tag{1.5}$$

This assumes the refractivity, $\mathbf{N}$, is a linear function of the bending angles α, of the form $\mathbf{N} = \mathbf{A}\alpha$. The expression accounts for the errors in the bending angle profile, but does not include errors associated with the statistical optimization and the extrapolation of the bending angle profile to infinity.

Figure 1.9 shows the vertical profile of the standard deviation of the implied refractivity errors in the northern hemisphere for both Metop-A and COSMIC measurements using Eq.1.5. The thick lines denote the setting measurements and the thin lines are for rising measurements. The percentage errors in refractivity are smaller than for bending angles, and this can be explained by $\mathbf{A}$. Lohmann (2005) interprets the Abel transform, $\mathbf{A}$, as a low pass filter, and demonstrates analytically that the filter response to sinusoidal bending angle pertubations with vertical wave number k, scales as $\propto 1/\sqrt{k}$.

In general, all of the refractivity uncertainty estimates are larger than the 0.2 % value assumed above the tropopause for the operational ROM SAF 1D-Var processing (see also Kursinski *et al.*, 1997). There is also a clear difference in the uncertainty estimates for the rising and setting Metop measurements between 10-20 km, which is similar to differences seen in the operational monitoring of the ROM SAF refractivity products. This has been discussed within the ROM SAF a number of times, and the possible impact of bending angle error correlations has been emphasized (Syndergaard, Pers. Comm. 2016). This suggestion has been largely confirmed here. Although the standard deviation of the bending angle errors are larger for rising Metop-A observations than setting (Figure 1.3), we have found that the refractivity error statistics differences are mainly caused by the broader positive bending angle correlations for rising Metop measurements attributed to the L2 extrapolation, shown in Figure 1.5. This dependence is illustrated in Figure 1.10, where two artificial "mixed" bending angle covariance matrices have been constructed and propagated through the Abel transform, $\mathbf{A}$. The first (MIX1) is composed of the rising bending angle error correlation matrix with the setting bending angle error standard deviation values, and the second (MIX2) is the setting bending angle error correlation matrix, with the rising bending angle error standard deviations. It is clear that the broader correlations for setting measurements account for most of the difference in the rising/setting uncertainty estimates, and this probably explains why it has been difficult to see problems in the standard deviation of bending angle departure statistics which subsequently arise in refractivity space. The broader bending angle error correlations suggest that more power is in the low fequency errors, and the Abel transform is not able to filter them out as effectively.

When considering the results shown in Figure 1.10, it is important to recognize that a refractivity value at a given height derived with an Abel transform, $\mathbf{A}$, is a weighted sum of all bending angle values above that height. Various rows of the Abel transform matrix, $\mathbf{A}$, are shown in Figure 1.11, revealing – as expected – a sharp peak value and a broad positive

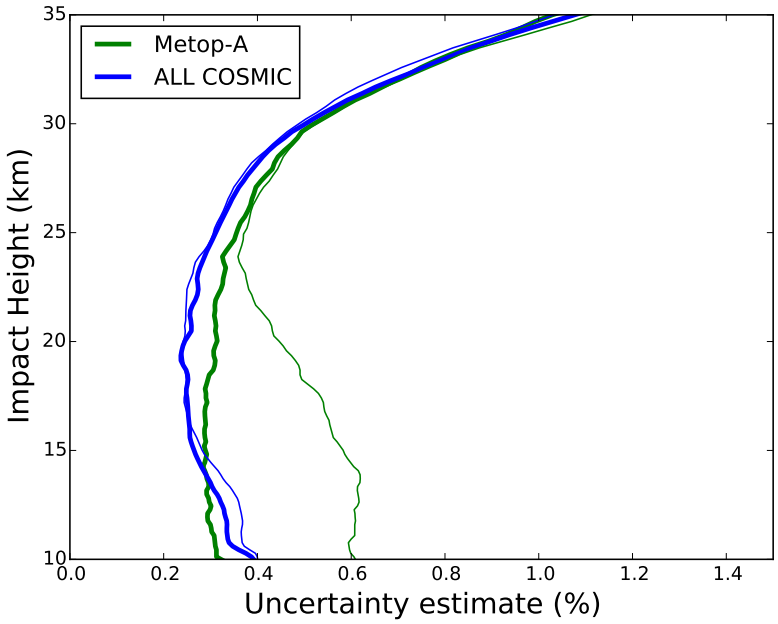

Figure 1.9: The standard deviation of the refractivity errors for Metop-A and the COSMIC measurements in the northern hemisphere estimated by propagating the bending angle error covariance matrix through the linearized Abel transform. Thick lines denote the setting observations and thin lines denote rising occultations.

tail. It is surprising that the row elements of $\mathbf{A}$ do not fall more quickly with impact height separation. Consider the contribution to a refractivity value at x, from bending angle value at $a \geq x$. The weighting given in the linear Abel transform will eventually fall towards zero, if $(a/x) >> 1$. However, for the typical GNSS-RO measurement geometry $a/x \sim 1$, because x is approximately given by the radius of the earth ($x \sim 6371$ km), and usually $a - x < 100$ km. This should be compared with the exponential decay of the bending angle values, approximately falling with the density scale-height, $H \sim 7$ km.

The shape of the Abel transform row vectors makes the refractivity values sensitive to positive bending angle error correlations. Conversely, negative error correlations in the vertical will tend reduce the refractivity error variance values because of cancellation of errors when performing the weighted sum. We can demonstrate this sensitivity to the correlations by modifying the bending angle correlation matrix, and then propagating it to refractivity space. Figure 1.12 shows the standard deviation of the refractivity error values for setting Metop-A measurements in the northern hemisphere. In addition to using the full bending angle correlation matrix (FULL), we have also assumed a diagonal bending angle correlation matrix (**C=I**)(DIAG). As might be expected, the refractivity error statistics with uncorrelated bending errors are smaller than those computed with a full correlation structure. However, more interesting results arise when we set parts of the bending angle correlation matrix to zero. If we set all off-diagonal terms to zero, except the one nearest to the diagonal (NEAREST, blue line), meaning the correlation matrix has a tridiagonal structure, we find the refractivity error estimates increase above those found with the full correlation matrix. Furthermore, if we keep just the 10 matrix elements closest to the diagonal (j=10, black line) and set the

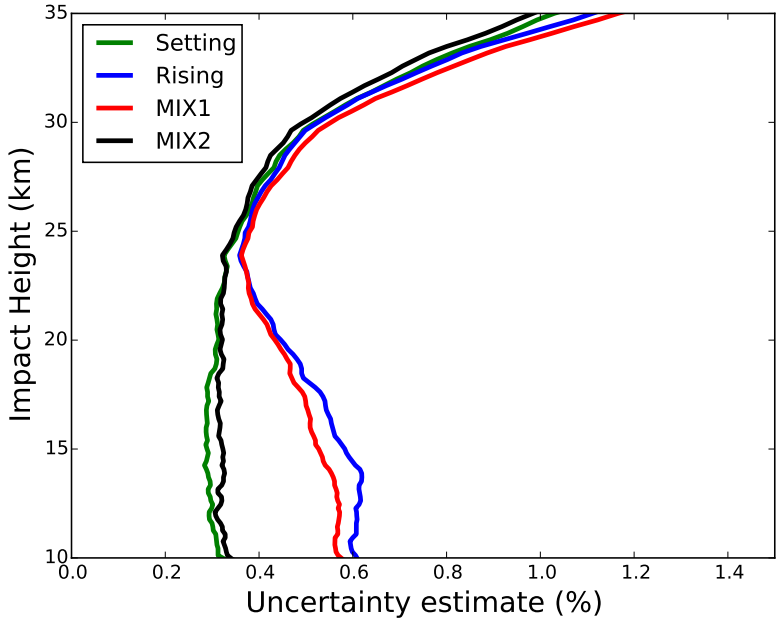

Figure 1.10: . The standard deviation of the refractivity errors for Metop-A rising and setting occultations. The artificial bending angle covariance matrix, MIX1, uses the bending angle standard deviations for setting measurements and the correlations from the rising occultations. Conversely the MIX2 matrix uses the standard deviations from rising occultations and correlations from setting occultations.

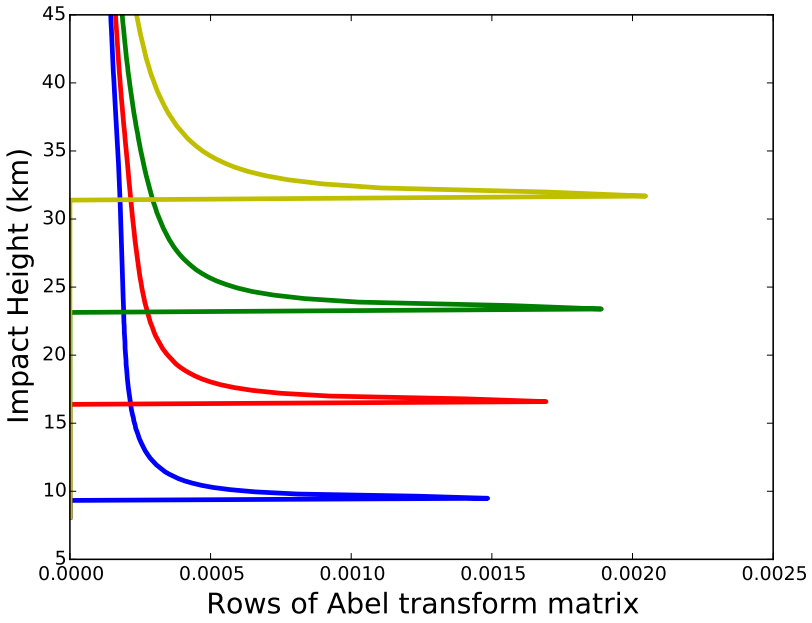

Figure 1.11: A selection of rows from the Abel transform matrix, $\mathbf{A}$. The peak value increases with height because the impact parameter separation increases.

others to zero, the errors fall below the results with the full correlation matrix. We can also obtain smaller error estimates than the DIAG case by setting all off-diagonal terms to -0.05 (not shown). Therefore, the broader bending angle correlations associated with both the full correlation matrix and the j=10 case, produce smaller refractivity error variances than the narrow correlation structure in the tridiagonal matrix. In addition, we can show that that increasing measurement error correlations do not necessarily imply a loss of information, with a toy model (see appendix).

The Abel transform also broadens the refractivity error correlations in the vertical (Steiner and Kirchengast, 2005), when compared to the bending angle correlations. We can demonstrate this initially by computing the refractivity error correlations *assuming* uncorrelated bending angle errors, as shown in Figure 1.13 where the observation height is near 13 km. We can compare the bending angle and refractivity correlations, as shown in Figure 1.14 and Figure 1.15 for setting and rising COSMIC and Metop-A measurements. For setting measurements, the COSMIC refractivity correlations are broader reflecting the broader bending angle correlations. It is surprising to see how much broader the Metop-A GRAS refractivity error correlations are for rising occultations than for setting measurements. This is because the Metop-A rising bending angle error correlations tend to a value of $\sim$ 0.2 below 20 km, as a result of the L1-L2 extrapolation. This sensitivity has been confirmed in numerical modelling. It is also apparent that exponentially decaying refractivity correlation matrix, suggested originally by Healy and Eyre (2000), and used in the operational ROM SAF 1D-Var products, should be revisited and different correlation matrices for rising and setting measurements should be considered.

Accurately modeling the vertical refractivity error correlations is essential if the bending angle and refractivity 1D-Var retrievals are to produce consistent results. This can be demon-

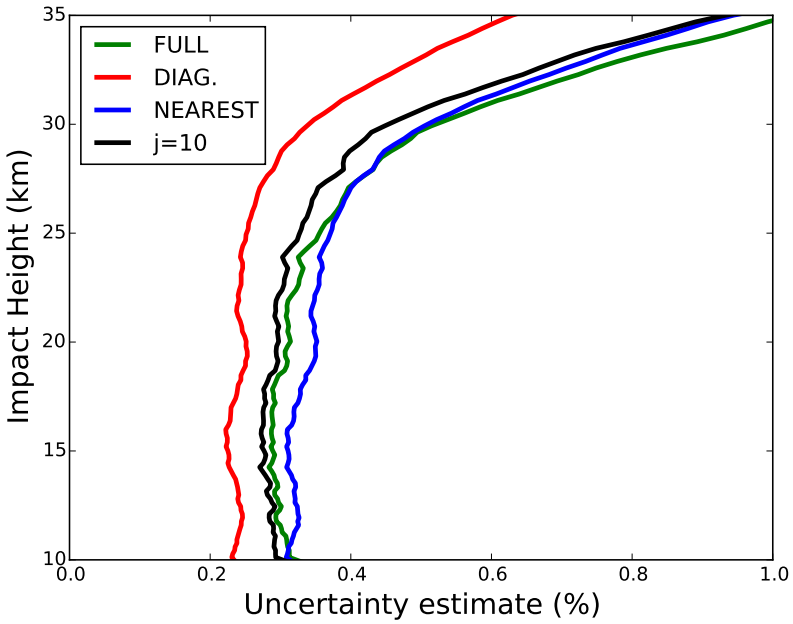

Figure 1.12: . The sensitivity of the refractivity error estimates to the bending angle correlation matrix. These are Metop-A setting measurements in the northern hemisphere. The FULL line is computed using the full bending angle correlation matrix, DIAG uses a diagonal correlation matrix, NEAREST uses a tri-diagonal correlation matrix, and j=10 uses just the 10 matrix elements closest to the diagonal, with the other matrix elements set to zero. The assumed bending angle error variances are the same in each case.

strated mathematically for a simplified linear system, assuming that the Abel transform matrix is square and invertible, meaning that no information is lost in the transform from bending angle to refractivity, $\mathbf{y_N} = \mathbf{A}\mathbf{y}_\alpha$ and $\mathbf{y}_\alpha = \mathbf{A^{-1}}\mathbf{y_N}$. (Note that information cannot be gained from a linear invertible transform). The observation component of the 1D-Var cost function for the refractivity vector can be written as,

$$\begin{aligned} J_o(\mathbf{y_N}) &= (\mathbf{y_N} - \mathbf{H_N}(\mathbf{x}))^{\mathbf{T}}\mathbf{R_N^{-1}}(\mathbf{y_N} - \mathbf{H_N}(\mathbf{x})) \\ &= (\mathbf{A}(\mathbf{y}_\alpha - \mathbf{A^{-1}}\mathbf{H_N}(\mathbf{x})))^{\mathbf{T}}\mathbf{R_N^{-1}}(\mathbf{A}(\mathbf{y}_\alpha - \mathbf{A^{-1}}\mathbf{H_N}(\mathbf{x}))) \\ &= (\mathbf{y}_\alpha - \mathbf{A^{-1}}\mathbf{H_N}(\mathbf{x}))^{\mathbf{T}}\mathbf{A^T}\mathbf{R_N^{-1}}\mathbf{A}(\mathbf{y}_\alpha - \mathbf{A^{-1}}\mathbf{H_N}(\mathbf{x})) \end{aligned} \tag{1.6}$$

where $\mathbf{H_N}$ computes the model refractivity and $\mathbf{R_N}$ is the refractivity error covariance matrix. If we assume the bending angle operator can be written as two steps, computing the model refractivity, $\mathbf{H_N}$, and then computing the bending, then $\mathbf{H} = \mathbf{H}_\alpha\mathbf{H_N}$. The observation component to the bending angle 1D-Var cost function is then

$$J_o(\mathbf{y}_\alpha) = (\mathbf{y}_\alpha - \mathbf{H}_\alpha\mathbf{H_N}(\mathbf{x}))^{\mathbf{T}}\mathbf{R}_\alpha^{\mathbf{-1}}(\mathbf{y}_\alpha - \mathbf{H}_\alpha\mathbf{H_N}(\mathbf{x})) \tag{1.7}$$

where $\mathbf{R}_\alpha$ is the bending angle error covariance matrix. Equating $\mathbf{A^{-1}} = \mathbf{H}_\alpha$, we see that Eq.1.6 and Eq.1.7 are the same if $\mathbf{R_N} = \mathbf{A}\mathbf{R}_\alpha\mathbf{A^T}$. Hence, the physical relationship relating the bending angles to the refractivity profile should be implicit in the off-diagonal terms of the matrix $\mathbf{R_N}$, rather than used explicitly in $\mathbf{H}_\alpha$ when assimilating bending angles. The off-diagonal terms of $\mathbf{R_N}$ should be monitored as well as the refractivity variances, because these should also constrain the 1D-Var solution. Ideally, changes in the EUMETSAT bending angle processing should also lead to updates in the $\mathbf{R_N}$ used in the 1D-Var. The key point is that the off-diagonal terms of $\mathbf{R_N}$ provide important physical information for the retrieval, and the 1D-Var results will be more robust to changes in the measurement error characteristics, if they are reflected in changes to the assumed refractivity error covariance matrix, $\mathbf{R_N}$.

We note that some information will be lost transforming from bending angle to refractivity, because *a priori* information is used. In practice, $\mathbf{R_N} = \mathbf{A}\mathbf{R}_\alpha\mathbf{A^T} + \mathbf{R_c}$ where $\mathbf{R_c}$ is the covariance of the *a priori*, climatological information required to estimate the refractivity profiles. However, this additional complexity is probably not important in the 10 - 20 km vertical interval, although it must be considered when assessing the refractivity error estimates above 30 km.

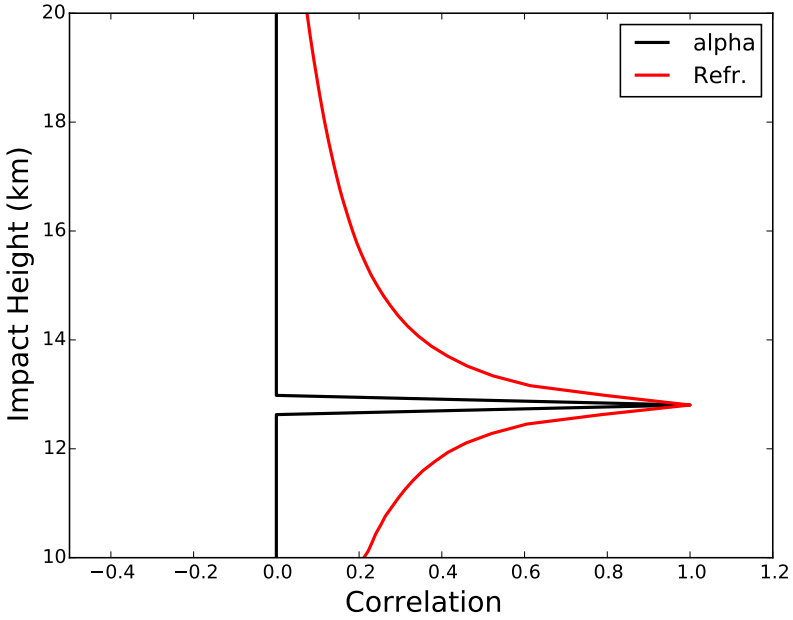

Figure 1.13: . The broadening of a “delta function” bending angle correlation by the Abel transform.

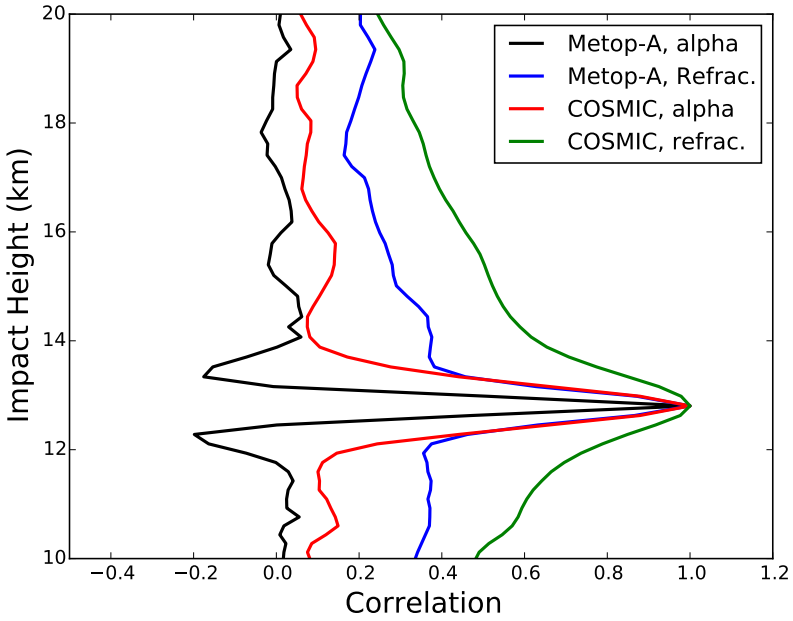

Figure 1.14: . The Metop-A GRAS and COSMIC bending angle and refractivity correlations near 13 km for setting occultations.

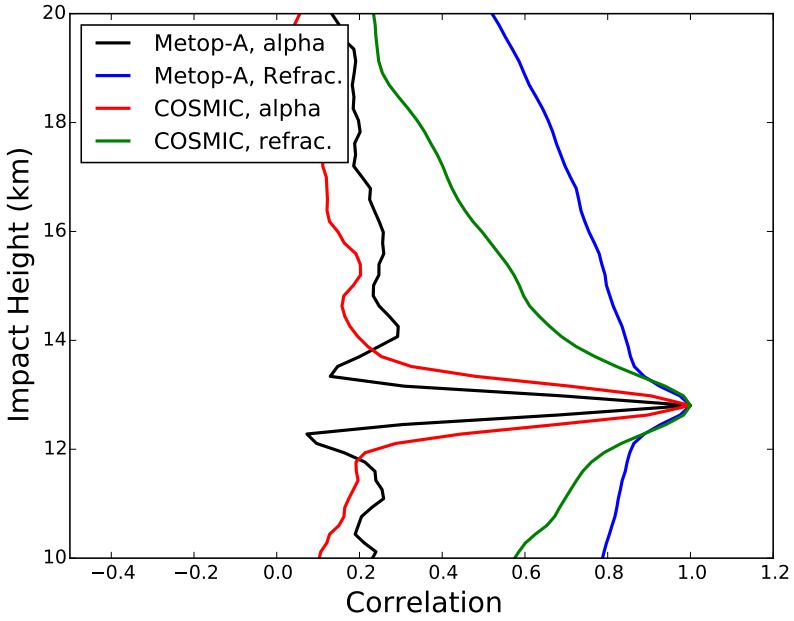

Figure 1.15: . The Metop-A GRAS and COSMIC bending angle and refractivity correlations near 13 km for rising occultations.

2 Summary

The NWP assimilation diagnostics have been used to estimate the error characteristics of the GNSS-RO measurements. The approach follows the work by Poli *et al.* (2009), and complements the various error propagtion studies (Kursinski *et al.* 1997; Syndergaard 1999; Steiner *et al.*, 1999; Steiner and Kirchengast 2005).

Estimates of bending angle error covariance matrices have been computed using the method suggested by Desrozier *et al.* (2005) for both the Metop GRAS and COSMIC measurements. The setting GRAS measurements have a familiar correlation structure, with negative lobes associated with a combination of a differentiation of the phase and a smoothing step. However, we have found significant differences in the vertical error correlations for rising and setting Metop GRAS measurements below 20 km. The rising measurement correlations are generally positive in the 10-20 km interval. This has a significant impact when mapped to refractivity space, and accounts for most of the difference in the rising/setting refractivity error statistics in the 10-20 km interval. The work also suggests the error model used in the ROM SAF 1D-Var retrievals should be reassessed.

3 Appendix: Some notes on correlated observation errors

Ignoring measurement error correlations can be particularly problematic if the observations are repeatedly measuring the same parameters. This is because the assimilation system assumes that random measurement errors are being reduced by repetition, and so the data is given too much weight in the analysis. In these circumstances, the variational analysis can have larger errors than the background forecast (e.g., Healy and White, 2005). However, introducing observation error correlations does not necessarily imply a loss of atmospheric state information at all scales. For example, Healy (2008) found that introducing GNSS-RO bending angle error correlations tended to increase the weight given to the measurements in the NWP system, and produce larger increments during the assimilation process.

In some cases, ignoring correlations can be a conservative approach. This can be demonstrated in a simple toy model. Consider estimating the two parameters, $\mathbf{x} = (x_1, x_2)^{\mathbf{T}}$ given a prior estimate $\mathbf{x_b} = (x_{1b}, x_{2b})^{\mathbf{T}}$ and observations $\mathbf{x_o} = (x_{1o}, x_{2o})^{\mathbf{T}}$. Let the uncertainty in the prior be $\mathbf{B} = \mathbf{I_2}$, where $\mathbf{I_2}$ is the 2 by 2 identity matrix, and let the observation uncertainty be given by the matrix,

$$\mathbf{R} = \begin{pmatrix} 1 & c \\ c & 1 \end{pmatrix} \tag{3.1}$$

If the forward operator is the identity matrix, $\mathbf{H} = \mathbf{I_2}$, it can be shown that the 1D-Var solution variance for both x_1 and x_2 is given by (see Figure 3.1),

$$\sigma^2(c) = \frac{(2-c^2)(1-c^2)}{(2-c^2)^2 - c^2} \tag{3.2}$$

The solution error variance is largest when the measurement error correlation is $c = 0$, with $\sigma^2(0) = 1/2$. Conversely, the solution error variances asymptote to their minimum value as the observation error correlation approaches unity, $\sigma^2(c \to \pm 1) \to 1/3$.

If the observations are assimilated erroneously, ignoring the actual error correlation, c, the solution error variance will be $\sigma^2 = 1/2$ and the actual solution error covariance matrix is,

$$\mathbf{A} = \begin{pmatrix} 1/2 & c/4 \\ c/4 & 1/2 \end{pmatrix} \tag{3.3}$$

using (Eq. 9, Healy and White 2005). Therefore, in this case we could potentially extract more information from the observations because of the error correlations. The more conservative approach of ignoring the correlations leads to $\sigma^2 = 1/2$.

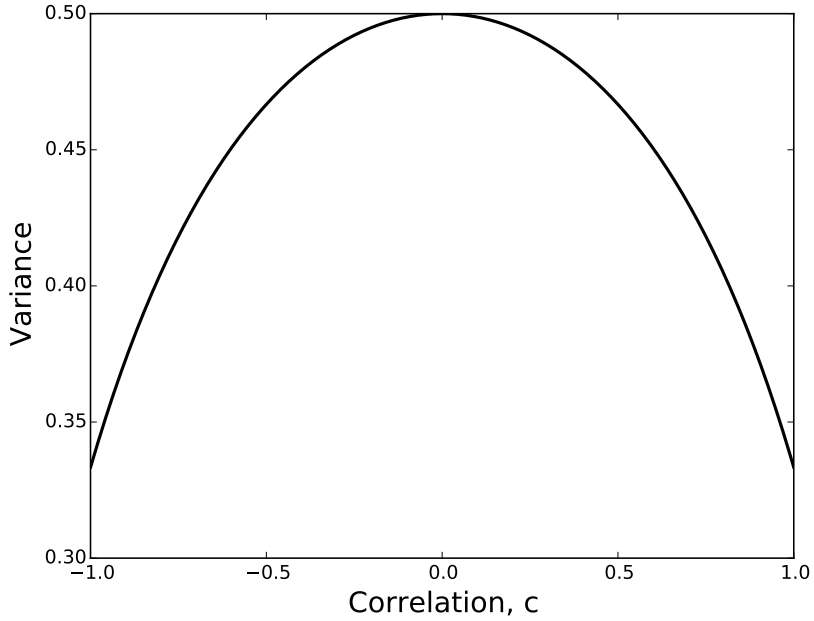

Figure 3.1: The variation of the solution error variance with measurement error correlation c based on Eq.3.2.

Acknowledgements

This work was carried out as part of EUMETSAT's Radio Occultation Meteorology Satellite Application Facility (ROM SAF) which is a decentralised operational RO processing center under EUMETSAT.

The comments from Dr Chris Burrows during the review stage have been extremely useful.

Bibliography

[1] Desroziers, G., L. Berre, B. Chapnik, and P. Poli, 2005: Diagnosis of observation, background and analysis-error statistics in observation space. *Q. J. R. Meteorol. Soc.*, **131**, 3385–3396.

[2] Healy, S. B., 2008: Assimilation of GPS radio occultation measurements at ECMWF. *ECMWF Proceedings of the GRAS SAF Workshop on Applications of GPS radio occultation measurements*, 99–109.

[3] Healy, S. B., and J. R. Eyre, 2000: Retrieving temperature, water vapor and surface pressure information from refractive–index profiles derived by radio occultation: A simulation study. *Q. J. R. Meteorol. Soc.*, **126**, 1661–1683.

[4] Healy, S. B., and A. A. White, 2005: Use of discrete Fourier transforms in the 1D-Var retrieval problem. *Q. J. R. Meteorol. Soc.*, **131**, 63–72. doi: 10.1256/qj.03.193.

[5] Jensen, A., M. Lohmann, H.-H. Benzon, and A. Nielsen, 2003: Full Spectrum Inversion of radio occultation signals. *Radio Sci.*, **38**, 1040, doi:10.1029/2002RS002763.

[6] Kursinski, E. R., G. A. Hajj, J. T. Schofield, R. P. Linfield, and K. R. Hardy, 1997: Observing earth's atmosphere with radio occultation measurements using the Global Positioning System. *J. Geophys. Res.*, **102**, 23.429–23.465.

[7] Lohmann, M. S., 2005: Application of dynamical error estimation for statistical optimization of radio occultation bending angles. *Radio Sci.*, **40**, RS3011, doi:10.1029/2004RS003117.

[8] Poli, P., P. Moll, D. Puech, F. Rabier, and S. B. Healy, 2009: Quality control, error analysis, and impact assessment of FORMOSAT-3/COSMIC in numerical weather prediction. *Terr. Atmos. Ocean*, **20**, 101–113.

[9] Steiner, A., and G. Kirchengast, 2005: Error analysis for GNSS radio occultation data based on ensembles of profiles from end-to-end simulations. *J. Geophys. Res.*, **110**, doi:10.1029/2004JD005251.

[10] Steiner, A., G. Kirchengast, and H. Ladreiter, 1999: Inversion, error analysis, and validation of GPS/MET occultation data. *Ann. Geophys.*, **17**, 122–138.

[11] Syndergaard, S., 1999: Retrieval analysis and methodologies in atmospheric limb sounding using the GNSS radio occultation technique. Scientific Report 99–6, Danish Meteorological Institute, Copenhagen.

ROM SAF (and GRAS SAF) Reports

SAF/GRAS/METO/REP/GSR/001	Mono-dimensional thinning for GPS Radio Occulation
SAF/GRAS/METO/REP/GSR/002	Geodesy calculations in ROPP
SAF/GRAS/METO/REP/GSR/003	ROPP minimiser - minROPP
SAF/GRAS/METO/REP/GSR/004	Error function calculation in ROPP
SAF/GRAS/METO/REP/GSR/005	Refractivity calculations in ROPP
SAF/GRAS/METO/REP/GSR/006	Levenberg-Marquardt minimisation in ROPP
SAF/GRAS/METO/REP/GSR/007	Abel integral calculations in ROPP
SAF/GRAS/METO/REP/GSR/008	ROPP thinner algorithm
SAF/GRAS/METO/REP/GSR/009	Refractivity coefficients used in the assimilation of GPS radio occultation measurements
SAF/GRAS/METO/REP/GSR/010	Latitudinal Binning and Area-Weighted Averaging of Irregularly Distributed Radio Occultation Data
SAF/GRAS/METO/REP/GSR/011	ROPP 1dVar validation
SAF/GRAS/METO/REP/GSR/012	Assimilation of Global Positioning System Radio Occultation Data in the ECMWF ERA-Interim Re-analysis
SAF/GRAS/METO/REP/GSR/013	ROPP PP validation
SAF/ROM/METO/REP/RSR/014	A review of the geodesy calculations in ROPP
SAF/ROM/METO/REP/RSR/015	Improvements to the ROPP refractivity and bending angle operators
SAF/ROM/METO/REP/RSR/016	Simplifying EGM96 Undulation calculations in ROPP
SAF/ROM/METO/REP/RSR/017	Simulation of L1 and L2 bending angles with a model ionosphere
SAF/ROM/METO/REP/RSR/018	Single Frequency Radio Occultation Retrievals: Impact on Numerical Weather Prediction
SAF/ROM/METO/REP/RSR/019	Implementation of the ROPP two-dimensional bending angle observation operator in an NWP system
SAF/ROM/METO/REP/RSR/020	Interpolation artefact in ECMWF monthly standard deviation plots
SAF/ROM/METO/REP/RSR/021	5th ROM SAF User Workshop on Applications of GPS radio occultation measurements
SAF/ROM/METO/REP/RSR/022	The use of the GPS radio occultation reflection flag for NWP applications
SAF/ROM/METO/REP/RSR/023	Assessment of a potential reflection flag product
SAF/ROM/METO/REP/RSR/024	The calculation of planetary boundary layer heights in ROPP
SAF/ROM/METO/REP/RSR/025	Survey on user requirements for ionospheric products

ROM SAF Reports are accessible via the ROM SAF website: http://www.romsaf.org